

Validating Sequential Monte Carlo for Gravitational-Wave Inference

M. J. Williams,¹* M. Karamanis,^{2,3,4} Y. Luo,⁵ U. Seljak^{2,3,4}

¹University of Portsmouth, Portsmouth, PO1 3FX, United Kingdom

²Berkeley Center for Cosmological Physics, UC Berkeley, CA 94720, USA

³Department of Physics, University of California, Berkeley, CA 94720, USA

⁴Lawrence Berkeley National Laboratory, One Cyclotron Road, Berkeley, CA 94720, USA

⁵School of Physics, Peking University, Beijing 100871, People's Republic of China

Accepted XXX. Received YYY; in original form ZZZ

ABSTRACT

Nested sampling (NS) is the preferred stochastic sampling algorithm for gravitational-wave inference for compact binary coalescences (CBCs). It can handle the complex nature of the gravitational-wave likelihood surface and provides an estimate of the Bayesian model evidence. However, there is another class of algorithms that meets the same requirements but has not been used for gravitational-wave analyses: Sequential Monte Carlo (SMC), an extension of importance sampling that maps samples from an initial density to a target density via a series of intermediate densities. In this work, we validate a type of SMC algorithm, called persistent sampling (PS), for gravitational-wave inference. We consider a range of different scenarios including binary black holes (BBHs) and binary neutron stars (BNSs) and real and simulated data and show that PS produces results that are consistent with NS whilst being, on average, 2 times more efficient and 2.74 times faster. This demonstrates that PS is a viable alternative to NS that should be considered for future gravitational-wave analyses.

Key words: gravitational waves – methods: data analysis – stars: neutron – stars: black holes – transients: black hole mergers – transients: neutron star mergers

1 INTRODUCTION

Bayesian inference is a cornerstone of gravitational-wave astronomy. It is used for a wide range of analyses, including characterising the compact binaries observed by the LIGO-Virgo-KAGRA Collaboration (LVK) (Abbott et al. 2023a). However, the nature of gravitational-wave data and these signals means that this inference can be complex, often requiring careful design and tuning of inference algorithms, and it can also be computationally expensive. This latter point is increasingly important as the sensitivity of LVK detectors improves (Abbott et al. 2016a) and the next-generation of detectors are built (Kalogera et al. 2021).

Different inference algorithms have been used within the gravitational-wave community for performing inference (Ashton et al. 2019; Veitch et al. 2015; Lange et al. 2018), however, nested sampling (NS) (Skilling 2004, 2006) is currently the de facto algorithm for most analyses (Abbott et al. 2024, 2023a; Nitz et al. 2023; Wadekar et al. 2023). Nested sampling (NS) can handle the complex parameter space that results from the gravitational-wave likelihood, which often includes degeneracies and multimodality. It also provides an estimate of the Bayesian model evidence (marginalized likelihood) that can be used for Bayesian model selection when, for example, performing tests of general relativity (Abbott et al. 2021a).

Sequential Monte Carlo (SMC) methods (also known as particle filters) are an extension to importance sampling that have a wide range

of applications for solving particle filtering problems, including to Bayesian inference (Bernardo et al. 2011). These methods evolve a set of particles from an initial reference distribution (often the prior distribution) to a target distribution (often the posterior distribution) via a sequence of intermediate distributions. This sequence is typically constructed either by iteratively introducing data or annealing the target distribution using an effective temperature parameter (Doucet et al. 2001). This approach has several notable benefits; its adaptive nature makes it well suited to complex, multimodal problems whilst being inherently parallelizable. It also has connections to NS, Salomone et al. (2018) showed that NS can be reformulated in the SMC framework. These properties make such methods an interesting avenue for gravitational-wave inference, however, they have only seen limited use in this area (Karamanis et al. 2022b).

In this paper, we validate sequential Monte Carlo for analysing gravitational-wave signals from compact binary coalescences (CBCs) and compare it to results obtained with a NS algorithm. The paper is structured as follows: in sections 2 and 3 we review the fundamentals of gravitational-wave inference for CBCs and SMC; in section 4 we describe the specific SMC algorithm we use, pocomc, and the changes made to it; in section 5 we validate pocomc using simulated data and compare results to those obtained using the NS algorithm, dynesty; in section 6 we apply pocomc to real CBC events from LVK observing runs; and in section 7 we summarise our findings.

* E-mail: michael.williams3@port.ac.uk

2 GRAVITATIONAL-WAVE INFERENCE

For **CBCs**, the observed strain data $\tilde{d}(f)$ is typically modelled in the frequency domain in terms of a frequency-dependent signal $\tilde{h}_\theta(f)$ with parameters θ , and frequency-dependent noise $\tilde{n}(f)$:

$$\tilde{d}(f) = \tilde{h}_\theta(f) + \tilde{n}(f). \quad (1)$$

In current analyses, the noise is assumed to be stationary, Gaussian and described by a one-sided **power spectral density (PSD)** $S_n(f)$. As such, the gravitational-wave likelihood is typically defined as a Gaussian function (Veitch et al. 2015; Thrane & Talbot 2019):

$$p(d|\theta, S_n(f)) \propto \exp\left\{-\frac{1}{2}\langle\tilde{d}(f) - \tilde{h}_\theta(f)|\tilde{d} - \tilde{h}_\theta(f)\rangle\right\}, \quad (2)$$

where $\langle a|b \rangle$ is the inner product (Cutler & Flanagan 1994; Veitch & Vecchio 2010)

$$\langle a|b \rangle = 2 \int_0^\infty \frac{\tilde{a}(f)\tilde{b}^*(f) + \tilde{a}^*(f)\tilde{b}(f)}{S_n(f)} df. \quad (3)$$

The signal in eq. (2) is modelled using a waveform approximant that models the predicted strain data as a function of parameters θ . This will include parameters that are intrinsic to the source, such as the masses and spins, and those which depend on the observer's location, the extrinsic parameters. Currently analyses predominantly use quasi-circular waveforms that include spin precession and high-order multipoles (Varma et al. 2019; Pratten et al. 2021; Ramos-Buades et al. 2023), this results in a 15-dimensional parameter space for **binary black holes (BBHs)** and a 17-dimensional parameter space for **binary neutron stars (BNSs)** — the two additional parameters quantify how each neutron star is deformed by tidal effects and are known as the tidal deformabilities $\lambda_{\{1,2\}}$.

In the current generation ground-based detectors, the resulting likelihood surface from eq. (2) can be multimodal and highly correlated in the 15 (17) parameters of interest. This, along with the computational cost associated with state-of-the-art waveforms (a few to hundreds of milliseconds per evaluation) and scaling with data duration, means inference for **CBC** signals can be computationally expensive, taking anywhere from hours to days.

When analysing real data, it is important to account for the frequency-dependent phase and amplitude error that arises from the imperfect calibration of the interferometric data (Cahillane et al. 2017; Viets et al. 2018). Therefore, we model the observed signal $\tilde{h}_{\text{obs}}(f)$ in terms of these unknown errors:

$$\tilde{h}_{\text{obs}}(f) = \tilde{h}_\theta(f)(1 + \delta A(f)) \exp[i\delta\phi(f)], \quad (4)$$

where $\delta A(f)$ and $\delta\phi(f)$ are the frequency-dependent amplitude and phase errors, respectively. These errors are expected to be small and smoothly varying (Viets et al. 2018), and are typically modelled using cubic spline polynomials with 10 nodes each (Farr et al. 2014). However, this introduces an additional 20 parameters per detector to the inference problem and any inference algorithm that is to be applied to real data must either include these parameters in the likelihood, or handle them via additional post-processing steps, see e.g. Payne et al. (2020). This increased dimensionality can prove particularly challenging for **NS** algorithms that rely on region-based proposal methods (Williams 2023).

As a result of the challenging nature of gravitational-wave inference, there has been extensive work into accelerating it, covering a wide range of approaches. Some focus on accelerating stochastic sampling and others focus on alternative methods such as simulation based inference (Dax et al. 2021; Bhardwaj et al. 2023) or non-Bayesian approaches (Fairhurst et al. 2023). In this work, we focus on the former which can be broadly be divided into two categories:

those that aim to reduce the cost of computing eq. (2) and those that aim to improve efficiency or scaling of the inference algorithm. This work falls into the latter category.

Within the area of the stochastic sampling algorithms, there has been extensive research into developing algorithms that are more efficient. Some works propose modifications to **NS** or **Markov Chain Monte Carlo (MCMC)** that, for example, incorporate normalizing flows (Williams et al. 2021; Ashton & Talbot 2021; Wong et al. 2023b; Prathaban et al. 2024). Others focus on developing new algorithms, many of which are based on importance sampling (Williams et al. 2023; Tiwari et al. 2023; Saleh et al. 2024). However, not all of these algorithms have been validated on the ‘full’ inference problem: analyses including higher-order multipoles, spin precession and calibration uncertainties. In this work, we aim to validate a new sampling algorithm for the full inference problem.

These algorithms are integrated into a range of gravitational-wave inference pipelines that implement the likelihood and associated data processing. Some pipelines use stochastic sampling algorithms — such as **bilby** (Ashton et al. 2019; Romero-Shaw et al. 2020), **LALInference** (Veitch et al. 2015), **PyCBC Inference** (Biver et al. 2019) and **cogwheel** (Roulet et al. 2022; Islam et al. 2022; Roulet et al. 2024) — whilst others use alternative algorithms including **RIFT** (Lange et al. 2018) and **DINGO** (Dax et al. 2021). The most recent **Gravitational Wave Transient Catalog (GWTC)**, **GWTC-3** (Abbott et al. 2023a) used a combination of **bilby** (Ashton et al. 2019)(with the **dynesty** sampler (Speagle 2020)) and **RIFT** (Lange et al. 2018).

3 SEQUENTIAL MONTE CARLO AND PERSISTENT SAMPLING

Sequential Monte Carlo (SMC) samplers iteratively transform an initial set of samples (called particles), typically drawn from the prior distribution, into a set of samples representing the target posterior distribution through a sequence of intermediate steps. A common and effective strategy to define these intermediate distributions is temperature annealing. One can conceptualize the likelihood function $p(d|\theta)$ as being gradually introduced. This is controlled by an inverse temperature parameter, β_t , that increases from $\beta_1 = 0$ (where the distribution is simply the prior) to $\beta_T = 1$ (where the distribution is the full posterior). At each step t , the intermediate distribution $p_t(\theta)$ is defined as:

$$p_t(\theta) = \frac{p(d|\theta)^{\beta_t} p(\theta)}{Z_t}, \quad (5)$$

where $p(\theta)$ is the prior and $Z_t = \int p(d|\theta)^{\beta_t} p(\theta) d\theta$ is the normalization constant (or evidence) at that temperature. Thus, $p_1(\theta)$ is the prior $p(\theta)$ (since $p(d|\theta)^0 = 1$), and $p_T(\theta)$ is the target posterior $p(\theta|d) \propto p(d|\theta)p(\theta)$. The final normalization constant Z_T is the standard Bayesian evidence. This gradual “annealing” process is particularly advantageous as it facilitates the algorithm’s navigation of complex likelihood surfaces. Such surfaces may feature multiple, well-separated modes (peaks) or narrow, convoluted ridges, which can be difficult for algorithms attempting to sample the posterior directly, as they risk becoming trapped in a single local optimum, thereby failing to map the full posterior landscape. Temperature annealing specifically addresses the challenge of multimodality because, at low β_t values (corresponding to high effective temperatures), the posterior landscape is significantly broadened and smoothed. In this flattened state, the probabilistic barriers that might ordinarily isolate different modes are substantially reduced.

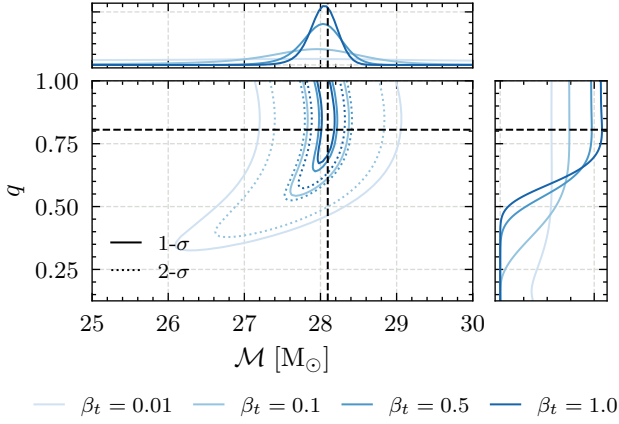


Figure 1. Annealed one- and two-dimensional posterior distributions (see eq. (5)) for chirp mass (M) and mass ratio (q) for a GW150914-like injection in zero-noise at four different inverse temperatures (β_t). The injection was simulated in a two-detector network using IMRPhenomPv2. The same waveform was used when computing the likelihood and all other parameters were fixed to the injected values except for the phase at coalescence, which was analytically marginalized (Thrane & Talbot 2019). The dashed vertical and horizontal lines indicate the injection parameters.

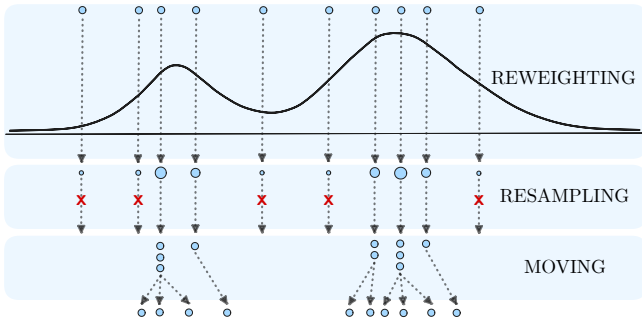


Figure 2. Single iteration t of the SMC algorithm demonstrating its three key operations, (i) reweighting, (ii) resampling, and (iii) moving. Particle positions are shown in 1D with particle weights represented by their relative size. Low-weight particles are discarded and high-weight ones are multiplied during resampling. The moving step diversifies the resampled population, yielding equally weighted and distinct particles.

This allows particles to traverse the parameter space more freely, making it easier for the sampler to discover and populate disparate regions of high probability that might otherwise be inaccessible. As β_t subsequently increases (i.e., the effective temperature decreases), these initially widespread particles, now hopefully distributed across various discovered modes, can then settle into and refine the characterization of each distinct mode as the features of the true posterior sharpen. As illustrated in fig. 1, at low β_t , the annealed posterior is broad, which simplifies initial exploration; as β_t increases, the distribution progressively concentrates, converging towards the true posterior and its potentially complex modal structure.

To transition the N particles, $\{\theta_{t-1}^i\}_{i=1}^N$, from approximating distribution $p_{t-1}(\theta)$ to approximating the next distribution $p_t(\theta)$, standard SMC algorithms employ three key operations (illustrated in fig. 2) at each iteration t :

- (i) **Reweighting:** Each particle θ_{t-1}^i , which was a sample from

$p_{t-1}(\theta)$, is assigned an importance weight. This weight quantifies how well the particle fits the new target distribution $p_t(\theta)$ compared to how it fit the old one $p_{t-1}(\theta)$. The unnormalized weight for particle i is given by

$$w_t^i = p(d|\theta_{t-1}^i) \beta_t - \beta_{t-1}, \quad (6)$$

(derived from $p_t(\theta_{t-1}^i)/p_{t-1}(\theta_{t-1}^i)$). These weights guide the particle population towards regions of higher probability under the new, more concentrated distribution $p_t(\theta)$. The normalized weights W_t^i are proportional to w_t^i . The ratio of the normalization constants, Z_t/Z_{t-1} , is estimated as the average of these unnormalized weights:

$$\frac{\hat{Z}_t}{\hat{Z}_{t-1}} = \frac{1}{N} \sum_{j=1}^N w_t^j. \quad (7)$$

Given that $Z_1 = 1$ (if the prior is normalized), this allows for an iterative estimation of the final evidence $Z_T = Z_1 \times (\hat{Z}_2/\hat{Z}_1) \times \dots \times (\hat{Z}_T/\hat{Z}_{T-1})$. The temperature β_t is often determined adaptively at each step by, for example, requiring that the **effective sample size (ESS)** (Kish 1965) of the weighted particles remains above a certain threshold, ensuring sufficient diversity of weights.

(ii) **Resampling:** After reweighting, some particles will have very low weights, indicating they are in regions of lesser importance for $p_t(\theta)$. To focus computational effort efficiently, a resampling step is performed: N new particles are drawn (with replacement) from the current set $\{\theta_{t-1}^i\}$ with probabilities proportional to their normalized weights $\{W_t^i\}$. This step tends to discard particles with low weights and replicate those with high weights, thereby concentrating the particle population in the more relevant regions of the parameter space for $p_t(\theta)$.

(iii) **Moving:** The resampling step can lead to multiple identical copies of high-weight particles. To diversify the particle population and allow them to explore the current distribution $p_t(\theta)$ more thoroughly, each newly resampled particle $\tilde{\theta}_t^i$ is then perturbed or "moved". This is typically done by applying an **MCMC** kernel, \mathcal{K}_t , for one or more steps, where \mathcal{K}_t is chosen to have $p_t(\theta)$ as its stationary distribution. This step, resulting in the updated particles $\theta_t^i \leftarrow \mathcal{K}_t(\tilde{\theta}_t^i)$, helps the particles explore the local landscape of $p_t(\theta)$ and resolve degeneracies. The choice of **MCMC** kernel (e.g., random-walk Metropolis (Metropolis et al. 1953), Hamiltonian Monte Carlo (Neal 2011)) can be adapted based on the properties of the current particle set, such as their empirical covariance, which is an advantage of the **SMC** framework.

Standard **SMC** addresses many shortcomings of simpler importance sampling; however, it still has limitations, particularly related to the fixed number of particles, which can lead to high variance in estimates and challenges like particle impoverishment (loss of diversity after resampling). As such, various modifications to this standard algorithm have been proposed. In this work, we consider one specific approach called **persistent sampling**. For an in-depth introduction to **SMC**, see Doucet et al. (2001).

Persistent sampling (PS), introduced by Karamanis & Seljak (2024), is an extension of **SMC** specifically designed to address significant limitations of standard **SMC** such as particle impoverishment and mode collapse, especially when computational resources are constrained. While **persistent sampling (PS)** also navigates a sequence of annealed distributions $p_t(\theta)$, its principal innovation is its particle management strategy. Instead of discarding particles from previous iterations ($t' < t$) after each resampling phase, **PS** systematically retains and reuses particles from all prior iterations. This process constructs a growing, weighted ensemble of particles that are

all utilized to represent the target distribution at the current iteration t .

The underlying mechanism involves treating the accumulated particles from all previous iterations $s = 1, \dots, t-1$ (a total of $(t-1) \times N$ particles if N particles are generated per iteration) as approximate samples from a mixture distribution

$$\tilde{p}_t(\theta) = \frac{1}{t-1} \sum_{s=1}^{t-1} p_s(\theta). \quad (8)$$

Reweighting is then performed using principles from multiple importance sampling, assigning new weights to all these $(t-1) \times N$ historical particles so that they collectively target the current distribution $p_t(\theta)$. From this much larger, combined pool, N new active particles are resampled, which are then diversified through the standard moving step.

The "persistent" methodology, as implemented in **PS**, offers substantial advantages, both as an enhancement to standard **SMC** techniques and when compared to other classes of algorithms such as **NS**.

PS significantly enhances standard **SMC** methodologies by systematically leveraging a growing, persistent pool of all previously generated particles. This core strategy leads to several key improvements (Karamanis & Seljak 2024): **PS** achieves higher accuracy efficiently, as reweighting historical particles utilizes cached likelihood values, thereby avoiding new computationally expensive likelihood evaluations for these samples. The resulting larger and more diverse particle ensemble allows for the construction of more robust posterior approximations, directly mitigating common **SMC** issues such as particle impoverishment and mode collapse. Consequently, estimates of marginal likelihood and posterior expectations typically exhibit significantly lower variance. Furthermore, the process of resampling active particles from this extensive persistent pool yields new particles that are naturally more distinct and less correlated, which alleviates the diversification burden on the **MCMC** moving step and facilitates more stable and efficient adaptation of its transition kernels.

When contrasted with other methodologies like **NS**, **PS** with annealing also presents several distinct advantages:

- **Highly Efficient Parallelization:** The **MCMC** moving step, central to **PS** (inherited from **SMC**), is embarrassingly parallel. This allows for near-linear performance scaling with the number of processing units, offering a significant advantage over methods like **NS** which often have more constrained parallelization capabilities.

- **Favourable High-Dimensional Scaling:** **PS** with temperature annealing reportedly exhibits computational cost scaling with parameter space dimensionality (D) as approximately $O(D^{1/2})$ (Chopin & Papaspiliopoulos 2020). This offers a potential performance advantage in high-dimensional problems compared to algorithms with less favourable scaling (e.g., the typical $O(D)$ scaling for **NS**), particularly when the posterior is significantly more concentrated than the prior.

- **Enhanced Exploration of Complex Posteriors via Annealing:** Temperature annealing systematically enables **PS** to effectively navigate complex, multimodal likelihoods. It allows particles to initially explore a smoothed landscape (at low β_t), aiding the discovery of disparate modal regions before the posterior sharpens as $\beta_t \rightarrow 1$. While **NS** also addresses multimodality, the annealing mechanism in **PS** provides a structured, global-to-local exploration strategy.

- **Natural Termination and Online Learning Adaptability:** Unlike **NS**, the annealing process in **PS** has a clear termination point when β_t reaches its target (typically 1). Furthermore, the underly-

ing **SMC** framework inherent to **PS** directly supports online learning via data tempering (sequential data introduction), making it suitable for streaming data applications, a feature less readily available in standard **NS** implementations.

These characteristics establish **PS** as a robust, scalable, and efficient alternative for addressing complex Bayesian inference tasks, demonstrating superior performance compared to standard **SMC** and related variants, particularly under constrained computational budgets. This makes it an interesting candidate for gravitational-wave inference (Karamanis et al. 2022b). For a comprehensive description of the **PS** algorithm, its theoretical underpinnings, and empirical performance, readers are referred to Karamanis & Seljak (2024).

4 pocomc

In this work, we use a specific implementation of **PS**, called pocomc (Karamanis et al. 2022b,a), this includes the version of the algorithm described in Karamanis & Seljak (2024). pocomc includes several features that make it well suited to complex inference problems, such as gravitational-wave inference for **CBCs**. These include, but are not limited to:

- **Preconditioning with normalizing flows:** pocomc leverages normalizing flows (Kobyzev et al. 2019; Papamakarios et al. 2019) to apply a change-of-variables transformation (preconditioning) to the moving step. The preconditioning reduces the correlation between parameters, which improves the efficiency of the **MCMC** sampling and reduces the reliance on an appropriate choice of proposal distribution. This has parallels to how normalizing flows have been used in other sampling algorithms for gravitational-wave inference, such as *nessai* (Williams et al. 2021, 2023) and *fLowMC* (Wong et al. 2023a; Gabri e et al. 2022), which have been shown to improved sampling efficiency for gravitational-wave problems compared to standard algorithms Williams et al. (2021, 2023); Wong et al. (2023b).

- **t -preconditioned Crank-Nicolson MCMC:** pocomc implements the t -preconditioned Crank-Nicolson (tpCN) **MCMC** algorithm (Grumitt et al. 2024), an **MCMC** sampling scheme that is well suited to high-dimensional problems where the target distribution is non-Gaussian and that out-performs other, simpler **MCMC** methods. Karamanis & Seljak (2024) applied pocomc with this **MCMC** algorithm to range of challenging toy problems and demonstrated its robustness. This is particularly important since previous studies have shown that simpler **MCMC** algorithms are insufficient for gravitational-wave inference problems (Kulkarni & Capano 2021) and more complex algorithms are often required (Veitch et al. 2015; Ashton & Talbot 2021).

- **Parallelization:** as mentioned previously, the moving step in **SMC** is embarrassingly parallel — the speed-up scales approximately linearly with number of processes — and pocomc supports such parallelization. Furthermore, typical applications can use upwards of 1000 particles meaning that the algorithm can easily scale to hundreds of parallel processes. **NS**, in contrast, exhibits diminishing returns as the number of parallel process increases (Handley et al. 2015). In this work, we make use of the support for external parallelization and use the pool provided by *bilby*, though pocomc supports various forms of parallelization Karamanis (2024a).

- **User-specified number of posterior samples:** pocomc allows the user to specify the desired number of effective posterior samples independently of the number of particles for the **SMC** algorithm. This is achieved by drawing additional samples once the main **SMC** algorithm is complete and avoids the need to increase the number of

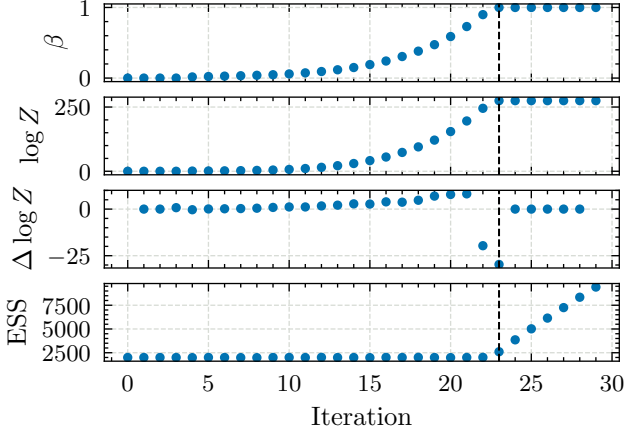


Figure 3. Evolution of the β parameter, log-evidence $\log Z$ and **ESS** of the particles when analysing GW150914_095045 using `pocomc`, this analysis includes calibration uncertainties. The β parameter is adaptively chosen at each iteration and slowly increases until $\beta = 1$, during this time, the **ESS** of particles is kept constant. Once $\beta = 1$ additional samples are drawn to reach the **ESS** specified by the user, 10,000 in this case. The results are discussed in detail in section 6.

particles. When using `pocomc` this is specified via the `n_total` argument, see the documentation for more details (Karamanis 2024a).

We also make a series of improvements to `pocomc` which are designed to handle certain characteristics of the gravitational-wave parameter space, however, they are not problem-specific. The changes are:

- **Sliced Iterative Normalizing Flows:** instead of the standard Masked Autoregressive Flows, we use Sliced Iterative Normalizing Flows (Dai & Seljak 2021). We find that these flows are better at handling multimodal distributions than the Masked Autoregressive Flows (Papamakarios et al. 2017) and Real Non-Volume Preserving flows (Dinh et al. 2016) previously available in `pocomc`. In the version used in this work, the flows are implemented in `sinflow` (Karamanis 2024b) and are used by default when running `pocomc`.
- **Boundary conditions:** since a number of the gravitational-wave parameters have periodic boundary conditions, we implement periodic boundary conditions in `pocomc`. Specifically, we map the angles to $[0, 2\pi)$ and apply a rotation such the mean is π . We find this reduces undersampling at the prior bounds for periodic parameters that can otherwise occur.

Figure 3 shows an example of how the inverse temperature parameter, β , evolves when applied to a **CBC** analysis. It initially evolves slowly whilst the sampler has yet to explore the bulk of the posterior, and then increases more rapidly at later iterations. The log-evidence follows a similar trend, rapidly increasing as $\beta \rightarrow 1$ but then decreasing over the final iterations as it converges to the final value.

In order to perform gravitational-wave analyses, we implement an interface between `pocomc` and the Bayesian inference library, `bilby` (Ashton et al. 2019; Romero-Shaw et al. 2020; Talbot et al. 2025) in the `pocomc-bilby` package (Williams 2025). This leverages the sampler-plugin interface in `bilby` to enable the user to run `pocomc` as they would any other sampler in `bilby` via the `run_sampler` interface or via `bilby_pipe`. The source code is available via PyPI and at <https://github.com/mj-will/pocomc-bilby> which also includes examples of how to run `pocomc` via `bilby`.

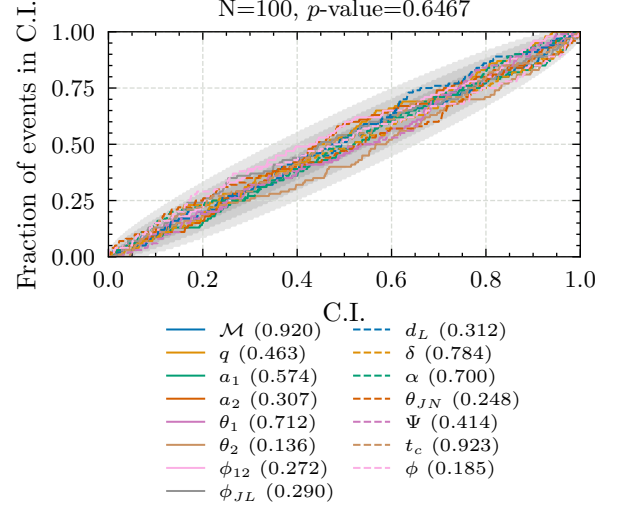


Figure 4. Probability-probability plot obtained using `pocomc` to analyse 100 simulated **BBH** signals in two-detector network consisting of LIGO Hanford and LIGO Livingston. The shaded regions denote the 1-, 2- and 3- σ bounds respectively. Per-parameter p -values are quoted, as well as the combined p -value computed using Fisher’s method (Fisher 1970).

5 VALIDATING `pocomc` FOR GRAVITATIONAL-WAVE INFERENCE

We validate `pocomc` using simulated data. All analyses are run using `bilby` and `bilby_pipe` (Ashton et al. 2019; Romero-Shaw et al. 2020; Talbot et al. 2025) and `pocomc-bilby` plugin described previously. Code to reproduce all of the analyses and the results are available in the accompanying data release (Williams et al. 2025a,b).

We simulate signals from compact binary coalescences in LIGO Livingston (L), LIGO Hanford (H) and Virgo (V) at O3 sensitivity Aasi et al. (2015); Acernese et al. (2015); Abbott et al. (2016a) and consider both three- (HLV) and two-detector (HL) networks. We compare our results with those obtained with `bilby` with the `dynesty` (Speagle 2020) nested sampler; we specifically use the modified version of `dynesty` included in `bilby`¹.

5.1 Binary black hole analyses

For **BBH** simulations, we employ the waveform approximant `IMRPhenomXPHM` (Pratten et al. 2021) and simulate 100 signals in eight seconds of coloured Gaussian noise. We randomly draw the parameters from the priors described in appendix A, which include detector-frame chirp masses in $[25, 35] M_{\odot}$. The resulting signals have a median network **signal-to-noise ratio** (SNR) of 8.1 and 8.7 in the two- and three-detector networks, respectively. We run the analyses with distance marginalization enabled and use 4 cores per analysis. We also use the detector-based sky parameterization (azimuth ϵ and zenith κ) and define the reference time at the detector with the highest SNR (t_{IFO}) (Romero-Shaw et al. 2020).

We tune the sampler settings for `pocomc` for the two-detector analyses, since we observe that these are more challenging than the three-detector analyses due to the correlations that arise in extrinsic parameters. These settings are detailed in table A3. Unlike **NS**,

¹ For details, see <https://bilby-dev.github.io/bilby/dynesty-guide.html>

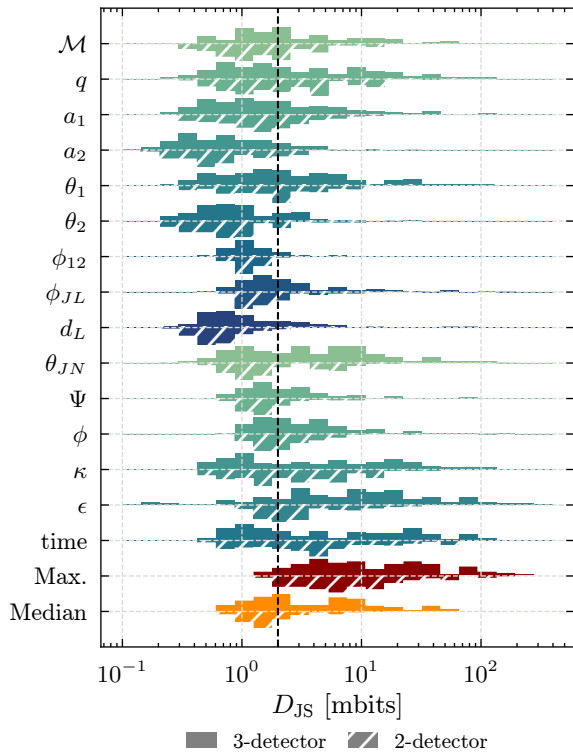


Figure 5. Per-parameter JSD between the posterior samples obtained with *pocomc* and *dynesty* for 100 simulated binary black hole signals when analysed in two- and three-detector networks. The upper and lower histograms show the three- and two-detector results respectively, the counts have been rescaled such the bin with the most counts has the same height between different parameters. The vertical dashed line shows the threshold proposed in *Ashton & Talbot (2021)*. ‘Max.’ and ‘Median’ denote the maximum and median JSD over all parameters per analysis, respectively. t_{IFO} denotes the time of coalescence as measured in the detectors with highest SNR .

pocomc allows the user to specify the desired number of effective posterior samples, we set this to 10,000 per event, however, for consistency with other samplers in *bilby*, we perform rejection sampling to produce **independent and identically distributed (i.i.d)** samples meaning that in practice we obtain fewer than 10,000 samples.

We perform probability-probability test for both network configurations and present the probability-probability plots for the two-detector case in fig. 4. Results for the three-detector case are included in appendix B. For each parameter, these plots show the fraction of events for which the injected value lies above the $n\%$ confidence interval. If the results are unbiased, then for $n\%$ confidence interval, $n\%$ of the events should lie above it (plus some uncertainty) and the line for a given parameter should lie near the diagonal. In both cases, the results obtained with *pocomc* are consistent with being unbiased; the results for all 15 parameters lie within the $3\text{-}\sigma$ uncertainties and the combined p -values computed using Fisher’s method (*Fisher 1970*) are greater than 0.05.

To further validate the results, we analyse the same injections using *dynesty*, as implemented in *bilby* with the settings detailed in table A4, and compare the posteriors to those obtained with *pocomc*. Probability-probability plots for the two- and three-detectors are shown in appendix B. With the settings used, *dynesty* passes both tests but the individual p -values for some of the parameters are lower than for *pocomc*, most notably for the declination δ and time of coalescence t_c . We attribute this to the signals being

relatively low SNR , including some that would likely not be detected by a matched-filter based search, which the settings are not tuned for. Furthermore, in *LVK* analyses *dynesty* would be run multiple times and the result combined together, thus improving the robustness of the results.

We quantify the difference between the inferred posterior samples by following previous works and computing the JSD between them. This measures the similarity between two probability distributions as a value between 0 and 1—larger values correspond to larger differences. The JSD is defined as

$$D_{\text{JS}}[p||q] = \frac{D_{\text{KL}}[p||m] + D_{\text{KL}}[q||m]}{2}, \quad (9)$$

where $D_{\text{KL}}(p||m)$ the **Kullback-Leibler Divergence (KLD)** and $m = 0.5(p + q)$ and the units will depend on the base on the logarithm used to compute D_{KL} . In this work, we use base 2 which corresponds to bits. Ideally, one would compute the n -dimensional JSD , however, this is challenging in practice and we instead follow previous studies and compute the JSD for the marginal posterior distributions. In practice, this requires fitting a kernel density estimator to each set of samples, computing the probability on a regular grid and then using these to compute the JSD .

We report the JSD between the marginal posterior distributions obtained with *pocomc* and *dynesty* in fig. 5. This shows that there are larger differences between the samplers for the extrinsic parameters with sky parameters, azimuth ϵ and zenith κ , and time of coalescence being the worse overall. *Ashton & Talbot (2021)* propose threshold of $10/n_{\text{eff}}$ mbit to determine if the samples are consistent or not, we compute the JSD using a random subset of 5,000 samples, so the corresponding threshold is 2 mbit. However, we note that the JSD values can change significantly depending on the settings used in its calculation, such as the number of bins and the type of kernel density estimator used². This means that while JSD is a useful comparative measure, comparing its absolute value between different works may not be informative, which brings into question the validity of the $10/n_{\text{eff}}$ mbit threshold. The 2 mbit threshold implies that many of the posterior distributions are inconsistent between the two samplers; however, the exact nature of the inconsistencies can vary greatly. We examine the posterior distributions and identify the most common differences:

- Different weights between modes in multimodal posterior distributions, this is most prevalent in sky and time parameters which at these SNRs are often highly multimodal. *pocomc* often assigns larger weights to secondary modes in e.g. the sky localization than *dynesty*;
- Different posterior probability at the prior bounds for intrinsic parameters that significantly rail against the prior bounds. This is a by-product of requiring the same priors for all injections when performing a probability-probability test and of the low SNRs being considered. In more realistic analyses, the prior bounds would be updated to avoid this;
- Narrow posteriors where the JSD calculation appears to break-down.

We therefore concluded the differences do not necessarily suggest that either sampler is incorrect but that analyses at low SNRs can be challenging. In practice, such analyses are uncommon since many of these injections would not be recovered by searches and, as mentioned

² Our implementation uses different kernel density estimators for periodic, bounded and unbounded parameters and we find this significantly impacts the JSD values compared to implementations do not account for boundaries.

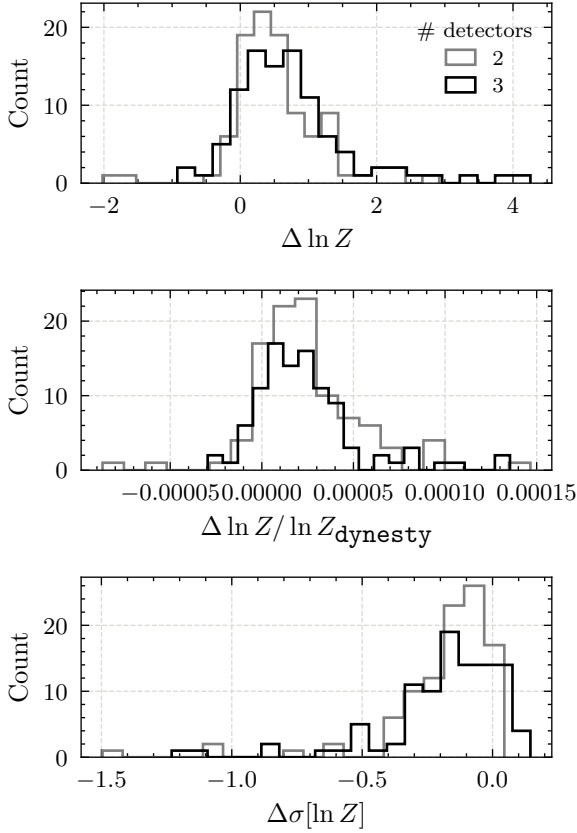


Figure 6. Comparison of the log-evidences estimated using *dynesty* and *pocomc* in 2- and 3-detector network configurations. The log-evidence estimates for *pocomc* were computed using 10,000 samples. All differences are defined as *dynesty*–*pocomc*. **Top:** absolute difference between estimated log-evidence. **Middle:** relative different difference in the log-evidence estimates. **Bottom:** absolute difference in the estimated uncertainty on the log-evidence.

previously, would combine multiple analyses to mitigate differences between different sampling realisations.

We can also compare the log-evidence estimates returned by each sampler. If the results are consistent, then any differences should be smaller than the associated uncertainty. However, since we observe differences in the inferred posterior distributions, we should expect to also see differences in the log-evidences. Figure 6 shows the distribution of absolute and relative differences in estimated log-evidences between *dynesty* and *pocomc*. The distribution is skewed towards positive differences, suggesting that *pocomc* tends to under-estimate the log-evidence compared to *dynesty* (or, equally *dynesty* over-estimates it). However, the relative difference shows that the differences are small compared to the log-evidence with a largest relative difference of less than 0.015%. Figure 6 also shows the absolute difference in estimated uncertainty on the log-evidence from each sampler. The uncertainty from *pocomc* is almost always larger than that from *dynesty* (the difference is negative) which is consistent with previous studies that showed that *NS* typically underestimates the uncertainty (Higson et al. 2018).

In figs. 7 and 8, we compare the efficiency and cost of the different analyses. For both samplers, we track the total number of likelihood evaluations and total wall time for each analysis. We note however that the wall time is less reliable as the analyses may have run on different hardware. Additionally, since the analyses do not produce

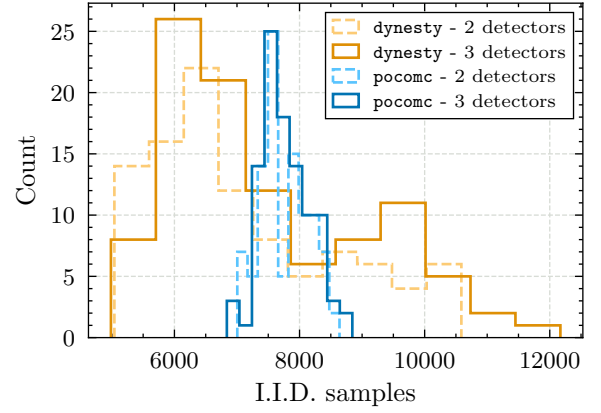


Figure 7. Number of *i.i.d* posterior samples produced by *pocomc* and *dynesty* when analysing 100 simulated *BBH* events. *pocomc* was configured to return weighted samples with an *ESS* of 10,000, rejection sampling was then used to obtain *i.i.d* samples.

the same number of samples (see fig. 7), we compute the per-sample statistics. We present these results in fig. 8 for both the two- and three-detector runs. This shows that with chosen settings *pocomc* is between two to seven times more efficient in terms of likelihood evaluations than *dynesty*, which translates to a similar reduction in total wall time. The average efficiency improvement for two-detectors (three-detectors) is 1.92 ± 0.51 (2.09 ± 0.56) or, in terms of wall time 2.63 ± 0.93 (2.84 ± 1.04) per sample.

5.2 Binary neutron star analyses

We consider two regimes for *BNS* inference: fast inference suitable for low-latency analyses and slower, more robust inference for publication-quality analyses. In both cases, we use the *IMRPhenomPv2* (Hannam et al. 2014) waveform approximant (optionally with tidal parameters (Dietrich et al. 2019)) and leverage reduced-order modelling with *reduced order quadrature (ROQ)* to accelerate the gravitational-wave likelihood (Smith et al. 2016). Specifically, we use the *ROQ* bases described in Morisaki et al. (2023) which are available in Morisaki (2024) and are compatible with *bilby*.

We consider the same two- and three-detector configurations described previously, and simulate a 128-second GW190425-like *BNS* signal using *IMRPhenomPv2_NRTidalv2*. The signal is simulated with precessing spins and non-zero tidal parameters, the full set of injection parameters is described in table A2.

For the low-latency regime, we use more aggressive settings, excluding tidal parameters and perform analyses with precessing or aligned spins. This reduces the number of binary parameters from 17 to 15 when considering precession, and to 11 when assuming aligned spins. Further speed-ups could be achieved by using techniques such as those described in Morisaki & Raymond (2020) but since this would apply to both samplers, we do not include them here. We also use less stringent sampler settings for aligned analyses with *pocomc*, see table A4, and similarly to the *BBH* analyses, we also analyse the same signal using *dynesty*. We enable phase and distance marginalization for all analyses. We also restrict the prior on polarization angle to $[0, \pi/2]$ since the *IMRPhenomP* family of waveforms does not include higher-order modes and consider spin magnitudes up to 0.4 (Harry & Hinderer 2018).

We compute the *JSD* between the posterior samples produced by each sampler, comparing only cases where the priors and parameters

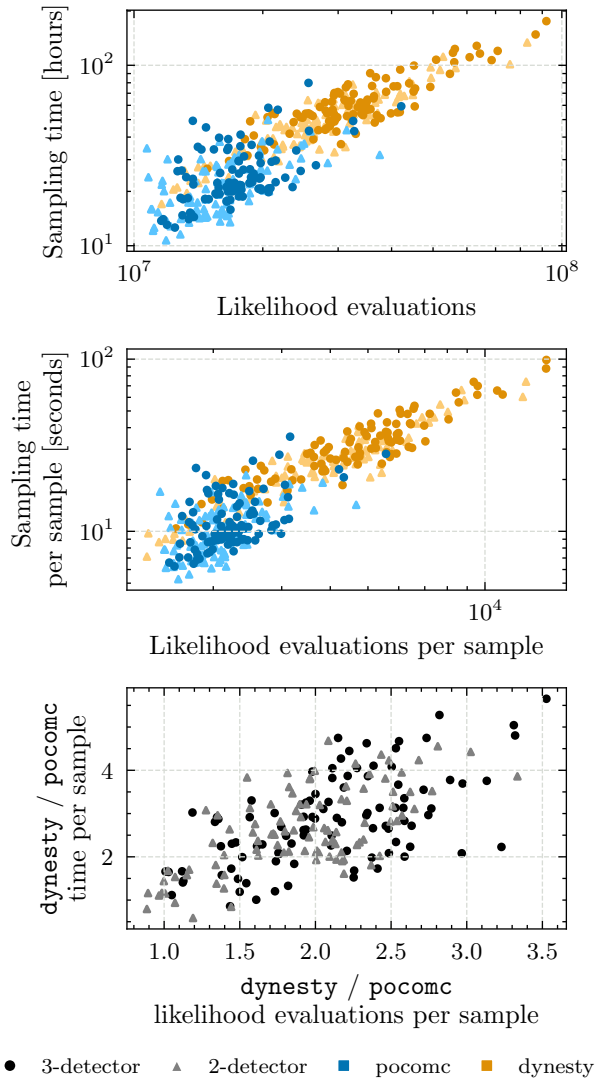


Figure 8. Comparison of the number of likelihood evaluations required and total wall time when sampling using pocomc (blue) and dynesty (orange) in two- and three-detector configurations. Circular markers denote three-detector results and triangular markers denote two-detector results. All analyses were run using four CPU cores. The average efficiency improvement for two-detectors (three-detectors) is 1.92 ± 0.51 (2.09 ± 0.56) or, in terms of wall time 2.63 ± 0.93 (2.84 ± 1.04)

being sampled are the same. Figure 9 shows the results without tidal parameters and those with tidal parameters are shown in appendix B. These results show that, unlike for the BBH analyses, the JSD values are broadly consistent for both samplers irrespective of the number of detectors and choice of aligned or precessing spins. However, when including tidal parameters in the analyses we observe larger differences and the inferred mass posteriors differ more than the analyses without tidal parameters. We cannot rule out the possibility that the dynesty results are not well converged but this suggests further investigation would be needed if pocomc were to be used for publication-quality BNS analyses.

We compare the sampling efficiency and cost, measured in terms of total number of likelihood evaluations and wall time, for each sampler and the various configurations for two-detector network in table 1. As expected, the results show a clear correlation between the sampling cost and complexity of the physics being modelled.

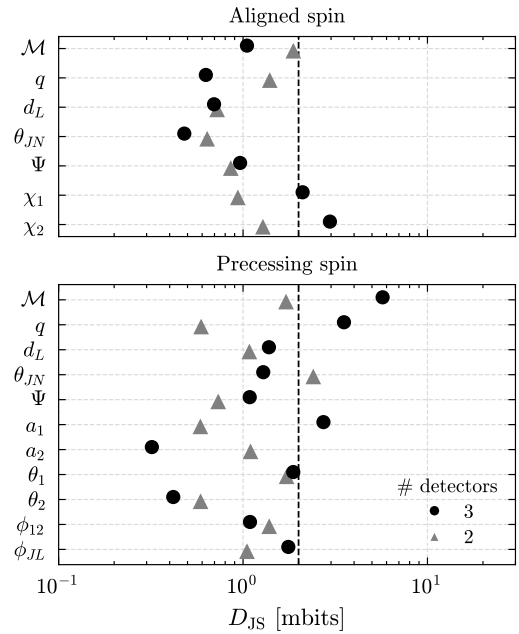


Figure 9. Mean JSD in millibits between posterior distributions obtained with dynesty and pocomc when analysing a simulated BNS signal as described in section 5.2. Results are shown for analyses with aligned and precessing spins, in both cases tidal effects are ignored, and for two- and three-detector networks. The JSD is computed 10 times per analysis using 5000 samples and the error bars show the standard deviation. The parameters are defined in table A1. The vertical dashed line shows the threshold proposed in Ashton & Talbot (2021)

However, there are significant differences between the two samplers; pocomc is two to three times more efficient than dynesty for the precessing analyses and the full precessing analyses with tidal parameters using pocomc are comparable in cost to the aligned-spin analyses without tides using dynesty. This efficiency improvement could allow low-latency analyses to include additional physics without increasing their cost compared to using dynesty.

6 APPLICATION TO REAL DATA

To further demonstrate the robustness of pocomc we analyse two gravitational-wave events from the first three LVK observing runs Abbott et al. (2019, 2021b, 2024, 2023a). We base our analyses on those performed in GWTCs-2.1 and -3 (Abbott et al. 2024, 2023a) and use the strain data that is publicly available via GWOSC (Abbott et al. 2021c, 2023b). We compare our results to the samples included in the data releases for these catalogues (LIGO Scientific Collaboration & Virgo Collaboration 2022; LIGO Scientific Collaboration et al. 2023). All analyses are run with twice per event and using 16 cores. Code to reproduce all of the analyses and the results are available in the accompanying data release (Williams et al. 2025a,b).

These analyses pose additional challenges compared to the simulated events, since the data may not be strictly stationary and Gaussian and additional calibration parameters described in section 2 must be included. We find that for these analyses pocomc performs better without preconditioning using the normalizing flow—sampling is slow and prone to over-constraining the posterior distribution. We attribute this to the increased dimensionality of the problem, which

Table 1. Comparison of the total number of likelihood evaluations, wall times and likelihood evaluation per sample when analysing a GW190425-like **BNS** using **pocomc** and **dynesty** with two-detector network. All analyses were run using 16 CPU cores and results are averaged over two runs. The equivalent table for a three-detector network is included in appendix B.

Sampler	Precession	Tides	Likelihood evaluations	Wall time [min]	Likelihood evaluations per sample
dynesty	X	X	3.3×10^7	167.3	7273
pocomc	X	X	2.4×10^6	34.99	589.7
dynesty	X	✓	3.8×10^7	295.9	6686
pocomc	X	✓	4.5×10^6	34.21	1140
dynesty	✓	X	4.1×10^7	303	7174
pocomc	✓	X	1.9×10^7	272.8	2417
dynesty	✓	✓	3.3×10^7	346.1	5395
pocomc	✓	✓	2.0×10^7	153.4	2556

makes effectively training the normalizing flow with the same number of samples challenging. We leave addressing this to future work.

GW150914_095045 was the first **BBH** detected by the **LVK** and is considered a ‘vanilla’ **BBH** with source frame component masses of $36 M_{\odot}$ and $29 M_{\odot}$ (Abbott et al. (2016b)). With **pocomc**, the analyses took on average 9 hours to complete, produced 7781 samples after rejection sampling, and required of order 20 million likelihood evaluations to converge. The inferred masses and spin parameters and subset of the extrinsic parameters are shown in figs. 10 and 11. These show overall agreement between the results obtained with **pocomc** and included in the **GWTC-2.1** data release. This demonstrates that **pocomc** is robust to the inclusion of additional calibration parameters. Furthermore, comparing to the results shown in fig. 8, we see that the inclusion of the calibration parameters has not significantly impacted the number of likelihood evaluations **pocomc** requires.

GW200129_065458 was a three-detector **BBH** merger detected in the third **LVK** observing run that shows evidence for spin-precession (Hannam et al. 2022) and has been the subject of many analyses, e.g. Payne et al. (2022); Macas et al. (2024). When analysed with **pocomc**, the analyses took on average 21 hours, required approximately 24 million likelihood evaluations and produced 7277 samples after rejection sampling. The posterior distributions from this analysis are compared to those included in the **GWTC-3** data release (LIGO Scientific Collaboration et al. 2023) in figs. 12 and 13, our results are consistent with those produced by the **LVK** but find additional support for the heavier mode at approximately $40 M_{\odot}$ and for larger values of the precessing spin parameter, χ_p . The extrinsic parameters show better agreement. Upon further examination, we find various differences in the analyses that could explain the differences in inferred intrinsic parameters. The Bayesian evidences for the noise-only hypothesis differ between the two results, suggesting differences in the data being analysed. Whilst both analyses use the same codes and waveform approximant, the exact versions differ, in particular the version of **IMRPhenomXPHM** used in our analyses contains several updates compared to **GWTC-3**.

7 CONCLUSIONS

In this work, we have demonstrated that **SMC** is a robust tool for performing gravitational-wave inference for **CBC** signals and a viable alternative to **NS**. In particular, we used **pocomc**, an **SMC** sampler that implements **PS**, an extension to the standard **SMC** that addresses some of its main shortcomings, and applied it to a range of different **CBC** analyses.

Initially, we test **pocomc** on a series of simulated signals: 100

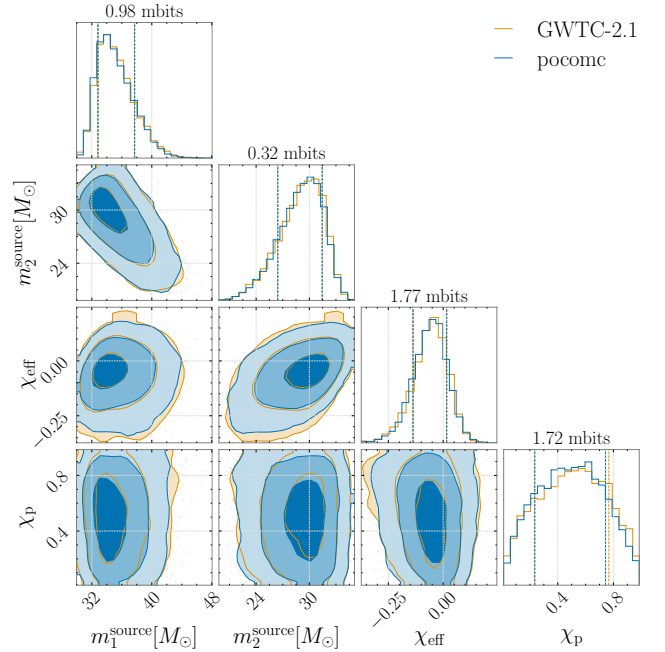


Figure 10. Inferred source frame component masses m_1^{source} and m_2^{source} , effective spin χ_{eff} and precession parameter χ_p for GW150914_095045 using **pocomc** (blue). Results are compared against those released by the **LVK** in **GWTC-2.1** (blue). The two-dimensional plots show the 1-, 2- and 3- σ contours. The vertical dashed line shows the 1- σ confidence interval. The **JSD** in mbits between the 1-dimensional posterior distributions is quoted above each histogram.

BBH signals and one GW190425-like **BNS**. From these results, we conclude that:

- **pocomc** can robustly perform inference for **BBH** signals in two- and three-detector networks using waveforms that include precession and higher-order multipoles;
- compared to the standard sampler used by the **LVK**, **dynesty**, **pocomc**, is on average 2 times more efficient and 2.74 times faster whilst returning a more consistent number of samples;
- when applied to **BNS** signals, **pocomc** is significantly more efficient than **dynesty** and could therefore enable more complete analyses with the same latency.

In addition to these simulated tests, we also reanalyse two real events from **GWTCs-2.1** and **-3** with **pocomc**: GW150914 and

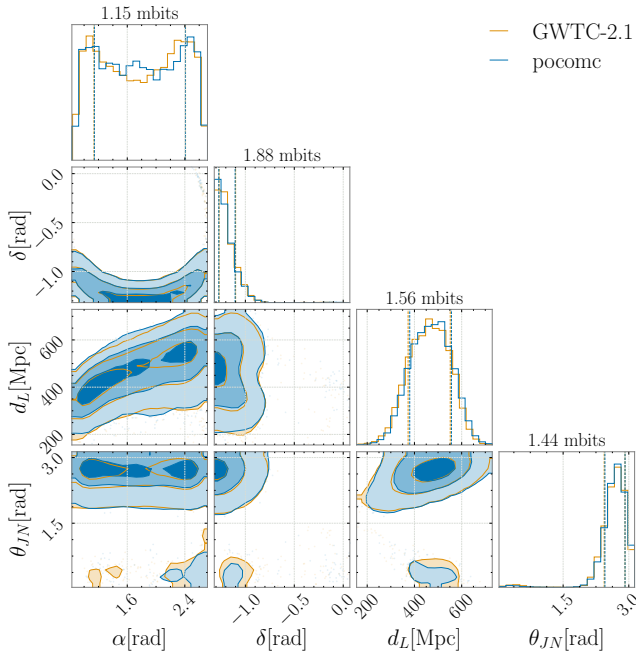


Figure 11. Inferred right ascension α , declination δ , luminosity distance d_L and inclination angle θ_{JN} for GW150914_095045 using pocomc (red). Results are compared against those released by the LVK in GWTC-2.1 (orange). The two-dimensional plots show the 1-, 2- and 3- σ contours. The vertical dashed line shows the 1- σ confidence interval. The JSD in mbits between the 1-dimensional posterior distributions is quoted above each histogram.

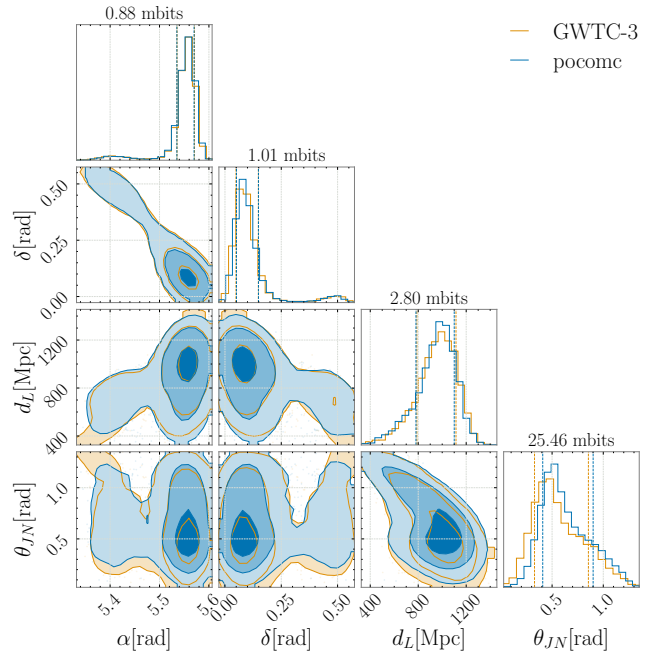


Figure 13. Inferred right ascension α , declination δ , luminosity distance d_L and inclination angle θ_{JN} for GW200129_065458 using pocomc (red). Results are compared against those released by the LVK in GWTC-3 (blue). The two-dimensional plots show the 1-, 2- and 3- σ contours. The vertical dashed line shows the 1- σ confidence interval. The JSD in mbits between the 1-dimensional posterior distributions is quoted above each histogram.

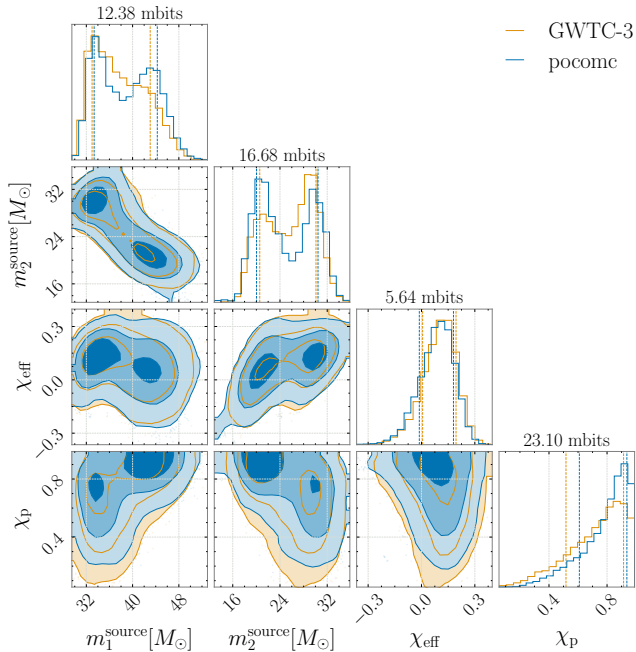


Figure 12. Inferred source frame component masses m_1^{source} and m_2^{source} , effective spin χ_{eff} and precession parameter χ_p for GW200129_065458 using pocomc (blue). Results are compared against those released by the LVK in GWTC-3 (orange). The two-dimensional plots show the 1-, 2- and 3- σ contours. The vertical dashed line shows the 1- σ confidence interval. The JSD in mbits between the 1-dimensional posterior distributions is quoted above each histogram.

GW200129. These analyses include additional parameters, 20 per-detector, to account for the inherent uncertainties in real data and these make inference more challenging. We show that pocomc is suitable for such analyses, producing results that are consistent with those released by the LVK, but this required disabling the preconditioning with normalizing flows. Further work is needed to improve the preconditioning to make it applicable to such analyses and to extensively verify that the settings used are robust across a wide range of events.

Looking forward, SMC should be considered when developing analyses for the next generation of ground- and space-based gravitational-wave detectors. In addition to this, SMC can easily leverage differentiable likelihoods via gradient-based Markov kernels such as Hamiltonian Monte Carlo (Neal 2011), whilst also improving efficiency of such kernels for multimodal problems and allowing for adaptive tuning of the kernel parameters (Buchholz et al. 2021). This makes SMC a prime candidate for development of gradient-based analyses.

ACKNOWLEDGEMENTS

The authors thank Ian Harry and John Veitch for providing feedback on the manuscript. MJW thanks Konstantin Leyde and Rahul Dhurkunde for helpful discussions, Charlie Hoy for advice on generating the BBH injections and Patricia Schmidt for advice on using IMRPhenomPv2_NRTidalv2. MJW acknowledges support from ST/X002225/1, ST/Y004876/1 and the University of Portsmouth. MN and US acknowledge funding from NSF Award Number 2311559, and from the U.S. Department of Energy, Office of Science, Office of Advanced Scientific Computing Research under Contract

No. DE-AC02-05CH11231 at Lawrence Berkeley National Laboratory to enable research for Data-intensive Machine Learning and Analysis.

This document has been assigned LIGO Document No. LIGO-P2500231.

The authors are grateful for computational resources provided by the LIGO Laboratory and Cardiff University and supported by National Science Foundation Grants PHY-0757058 and PHY-0823459 and STFC grants ST/I006285/1 and ST/V005618/1. Additional numerical computations were carried out on the SCIAMA High Performance Compute (HPC) cluster which is supported by the ICG and the University of Portsmouth and on resources of the National Energy Research Scientific Computing Center (NERSC). This material is based upon work supported by NSF’s LIGO Laboratory which is a major facility fully funded by the National Science Foundation.

This work made use of the following software packages: `bilby` (Talbot et al. 2025), `bilby_pipe` (Ashton et al. 2019), `corner` (Foreman-Mackey 2016), `dynesty` (Speagle 2020), `LALSuite` (LIGO Scientific Collaboration 2018; Wette 2020), `matplotlib` (Hunter 2007), `NumPy` (Harris et al. 2020), `pandas` (pandas development team 2020), `PESummary` (Hoy & Raymond 2021), `pocomc` (Karamanis et al. 2022a), `SciPy` (Virtanen et al. 2020), `seaborn` (Waskom 2021).

DATA AVAILABILITY

Interferometric data for the gravitational-wave events analysed and posterior samples produced by the LIGO-Virgo-KAGRA Collaboration are available via GWOSC (Abbott et al. 2021c, 2023b; LIGO Scientific Collaboration & Virgo Collaboration 2022; LIGO Scientific Collaboration et al. 2023). The data release including code to reproduce the figure and analyses as well as the simulated data and the full results is available online Williams et al. (2025a,b) and we also provide documentation for the data release at <http://gw-smc.michaeljwilliams.me>. `pocomc` is available at <https://github.com/minaskara/pocomc> and via PyPI. The `pocomc-bilby` interface is available at <https://github.com/mj-will/pocomc-bilby> (Williams 2025) and via PyPI.

REFERENCES

Aasi J., et al., 2015, *Class. Quant. Grav.*, 32, 074001
 Abac A. G., et al., 2024, *Astrophys. J. Lett.*, 970, L34
 Abbott B. P., et al., 2016a, *Living Rev. Rel.*, 19, 1
 Abbott B. P., et al., 2016b, *Phys. Rev. D*, 93, 122003
 Abbott B. P., et al., 2019, *Phys. Rev. X*, 9, 031040
 Abbott R., et al., 2021a, Tests of General Relativity with GWTC-3 (arXiv:2112.06861)
 Abbott R., et al., 2021b, *Phys. Rev. X*, 11, 021053
 Abbott R., et al., 2021c, *SoftwareX*, 13, 100658
 Abbott R., et al., 2023a, *Phys. Rev. X*, 13, 041039
 Abbott R., et al., 2023b, *Astrophys. J. Suppl.*, 267, 29
 Abbott R., et al., 2024, *Phys. Rev. D*, 109, 022001
 Acernese F., et al., 2015, *Class. Quant. Grav.*, 32, 024001
 Ashton G., Talbot C., 2021, *Mon. Not. Roy. Astron. Soc.*, 507, 2037
 Ashton G., et al., 2019, *Astrophys. J. Suppl.*, 241, 27
 Bernardo J., et al., 2011, *Bayesian statistics*, 8, 1
 Bhardwaj U., Alvey J., Miller B. K., Nissanke S., Weniger C., 2023, arXiv e-prints
 Biwer C. M., Capano C. D., De S., Cabero M., Brown D. A., Nitz A. H., Raymond V., 2019, *Publ. Astron. Soc. Pac.*, 131, 024503
 Buchholz A., Chopin N., Jacob P. E., 2021, *Bayesian Analysis*, 16, 745

Cahillane C., et al., 2017, *Phys. Rev. D*, 96, 102001
 Chopin N., Papaspiliopoulos O., 2020, An introduction to Sequential Monte Carlo, 1st ed. 2020. edn. Springer Series in Statistics, Springer, Cham, Switzerland
 Cutler C., Flanagan E. E., 1994, *Phys. Rev. D*, 49, 2658
 Dai B., Seljak U., 2021, in ICML Workshop on Invertible Neural Networks, Normalizing Flows, and Explicit Likelihood Models. <https://openreview.net/forum?id=VmwEpdsvHZ9>
 Dax M., Green S. R., Gair J., Macke J. H., Buonanno A., Schölkopf B., 2021, *Phys. Rev. Lett.*, 127, 241103
 Dietrich T., Samajdar A., Khan S., Johnson-McDaniel N. K., Dudi R., Tichy W., 2019, *Phys. Rev. D*, 100, 044003
 Dinh L., Sohl-Dickstein J., Bengio S., 2016, arXiv e-prints, p. arXiv:1605.08803
 Doucet A., De Freitas N., Gordon N., 2001, Sequential Monte Carlo methods in practice, pp 3–14
 Fairhurst S., Hoy C., Green R., Mills C., Usman S. A., 2023, *Phys. Rev. D*, 108, 082006
 Farr W. M., Farr B., Littenberg T., 2014, Technical Report T1400682, Modelling Calibration Errors In CBC Waveforms. LIGO
 Fisher R. A., 1970, in , Breakthroughs in statistics: Methodology and distribution. Springer, pp 66–70
 Foreman-Mackey D., 2016, *The Journal of Open Source Software*, 1, 24
 Gabrié M., Rotskoff G. M., Vanden-Eijnden E., 2022, *Proc. Nat. Acad. Sci.*, 119, e2109420119
 Grumitt R. D. P., Karamanis M., Seljak U., 2024, *Inverse Problems*, 40, 125023
 Handley W. J., Hobson M. P., Lasenby A. N., 2015, *MNRAS*, 453, 4384
 Hannam M., Schmidt P., Bohé A., Haegel L., Husa S., Ohme F., Pratten G., Pürrer M., 2014, *Phys. Rev. Lett.*, 113, 151101
 Hannam M., et al., 2022, *Nature*, 610, 652
 Harris C. R., et al., 2020, *Nature*, 585, 357
 Harry I., Hinderer T., 2018, *Class. Quant. Grav.*, 35, 145010
 Higson E., Handley W., Hobson M., Lasenby A., 2018, *Bayesian Analysis*, 13, 873
 Hoy C., Raymond V., 2021, *SoftwareX*, 15, 100765
 Hunter J. D., 2007, *Computing in Science & Engineering*, 9, 90
 Islam T., Roulet J., Venumadhav T., 2022, arXiv e-prints
 Kalogera V., et al., 2021, arXiv e-prints
 Karamanis M., 2024a, pocomc Documentation, <https://pocomc.readthedocs.io>
 Karamanis M., 2024b, sinflow, <https://github.com/minaskar/sinflow>
 Karamanis M., Seljak U., 2024, arXiv e-prints, p. arXiv:2407.20722
 Karamanis M., Nabergoj D., Beutler F., Peacock J. A., Seljak U., 2022a, arXiv preprint arXiv:2207.05660
 Karamanis M., Beutler F., Peacock J. A., Nabergoj D., Seljak U., 2022b, Monthly Notices of the Royal Astronomical Society, 516, 1644
 Kish L., 1965, Survey Sampling. John Wiley & Sons Inc.
 Kobayev I., Prince S. J. D., Brubaker M. A., 2019, arXiv e-prints, p. arXiv:1908.09257
 Kulkarni S., Capano C. D., 2021, *Phys. Rev. D*, 103, 104002
 LIGO Scientific Collaboration 2018, LIGO Algorithm Library - LALSuite, free software (GPL), doi:10.7935/GT1W-FZ16
 LIGO Scientific Collaboration Virgo Collaboration 2022, GWTC-2.1: Deep Extended Catalog of Compact Binary Coalescences Observed by LIGO and Virgo During the First Half of the Third Observing Run - Parameter Estimation Data Release, doi:10.5281/zenodo.6513631, <https://doi.org/10.5281/zenodo.6513631>
 LIGO Scientific Collaboration Virgo Collaboration KAGRA Collaboration 2023, GWTC-3: Compact Binary Coalescences Observed by LIGO and Virgo During the Second Part of the Third Observing Run — Parameter estimation data release, doi:10.5281/zenodo.8177023, <https://doi.org/10.5281/zenodo.8177023>
 Lange J., O’Shaughnessy R., Rizzo M., 2018, arXiv e-prints
 Macas R., Lundgren A., Ashton G., 2024, *Phys. Rev. D*, 109, 062006
 Metropolis N., Rosenbluth A. W., Rosenbluth M. N., Teller A. H., Teller E., 1953, *J. Chem. Phys.*, 21, 1087

Morisaki S., 2024, Reduced order quadrature bases for IMRPhe-
nomPv2_NRTidalv2, doi:10.5281/zenodo.14279382, <https://doi.org/10.5281/zenodo.14279382>

Morisaki S., Raymond V., 2020, *Phys. Rev. D*, 102, 104020

Morisaki S., Smith R., Tsukada L., Sachdev S., Stevenson S., Talbot C.,
Zimmerman A., 2023, *Phys. Rev. D*, 108, 123040

Neal R., 2011, in , Handbook of Markov Chain Monte Carlo. Chapman and
Hall/CRC, pp 113–162, doi:10.1201/b10905

Nitz A. H., Kumar S., Wang Y.-F., Kastha S., Wu S., Schäfer M., Dhurkunde
R., Capano C. D., 2023, *Astrophys. J.*, 946, 59

Papamakarios G., Pavlakou T., Murray I., 2017, *arXiv e-prints*, p.
[arXiv:1705.07057](https://arxiv.org/abs/1705.07057)

Papamakarios G., Nalisnick E., Jimenez Rezende D., Mohamed S., Lakshmi-
narayanan B., 2019, *arXiv e-prints*, p. [arXiv:1912.02762](https://arxiv.org/abs/1912.02762)

Payne E., Talbot C., Lasky P. D., Thrane E., Kissel J. S., 2020, *Phys. Rev. D*,
102, 122004

Payne E., Hourihane S., Golomb J., Udall R., Udall R., Davis D., Chatziioan-
nou K., 2022, *Phys. Rev. D*, 106, 104017

Prathaban M., Bevins H., Handley W., 2024, Accelerated nested sampling
with β -flows for gravitational waves ([arXiv:2411.17663](https://arxiv.org/abs/2411.17663))

Pratten G., et al., 2021, *Phys. Rev. D*, 103, 104056

Ramos-Buades A., Buonanno A., Estellés H., Khalil M., Mihaylov D. P.,
Ossokine S., Pompili L., Shiferaw M., 2023, *Phys. Rev. D*, 108, 124037

Romero-Shaw I. M., et al., 2020, *Mon. Not. Roy. Astron. Soc.*, 499, 3295

Roulet J., Olsen S., Mushkin J., Islam T., Venumadhav T., Zackay B., Zaldar-
riaga M., 2022, *Phys. Rev. D*, 106, 123015

Roulet J., Mushkin J., Wadekar D., Venumadhav T., Zackay B., Zaldarriaga
M., 2024, *Phys. Rev. D*, 110, 044010

Saleh B., Zimmerman A., Chen P., Ghattas O., 2024, *Phys. Rev. D*, 110,
104037

Salomone R., South L. F., Johansen A. M., Drovandi C., Kroese D. P., 2018,
arXiv e-prints, p. [arXiv:1805.03924](https://arxiv.org/abs/1805.03924)

Skilling J., 2004, *AIP Conf. Proc.*, 735, 395

Skilling J., 2006, *Bayesian Analysis*, 1, 833

Smith R., Field S. E., Blackburn K., Haster C.-J., Pürrer M., Raymond V.,
Schmidt P., 2016, *Phys. Rev. D*, 94, 044031

Speagle J. S., 2020, *Mon. Not. Roy. Astron. Soc.*, 493, 3132

Talbot C., et al., 2025, bilby-dev/bilby, doi:zenodo.14025463, <https://doi.org/10.5281/zenodo.14025463>

Thrane E., Talbot C., 2019, *Publ. Astron. Soc. Austral.*, 36, e010

Tiwari V., Hoy C., Fairhurst S., MacLeod D., 2023, *Phys. Rev. D*, 108, 023001

Varma V., Field S. E., Scheel M. A., Blackman J., Gerosa D., Stein L. C.,
Kidder L. E., Pfeiffer H. P., 2019, *Phys. Rev. Research.*, 1, 033015

Veitch J., Vecchio A., 2010, *Phys. Rev. D*, 81, 062003

Veitch J., et al., 2015, *Phys. Rev. D*, 91, 042003

Viets A., et al., 2018, *Class. Quant. Grav.*, 35, 095015

Virtanen P., et al., 2020, *Nature Methods*, 17, 261

Wadekar D., Roulet J., Venumadhav T., Mehta A. K., Zackay B., Mushkin J.,
Olsen S., Zaldarriaga M., 2023, New black hole mergers in the LIGO-
Virgo O3 data from a gravitational wave search including higher-order
harmonics ([arXiv:2312.06631](https://arxiv.org/abs/2312.06631))

Waskom M. L., 2021, *Journal of Open Source Software*, 6, 3021

Wette K., 2020, *SoftwareX*, 12, 100634

Williams M. J., 2023, PhD thesis, Glasgow U., doi:10.5525/gla.thesis.83924

Williams M. J., 2025, mj-will/pocomc-bilby: v0.1.0,
doi:10.5281/zenodo.15543727, <https://doi.org/10.5281/zenodo.15543727>

Williams M. J., Veitch J., Messenger C., 2021, *Phys. Rev. D*, 103, 103006

Williams M. J., Veitch J., Messenger C., 2023, *Mach. Learn. Sci. Tech.*, 4,
035011

Williams M. J., Karamanis M., Luo Y., Seljak U., 2025a, Validat-
ing Sequential Monte Carlo for Gravitational-Wave Inference - Code
Release, doi:10.5281/zenodo.15657234, <https://doi.org/10.5281/zenodo.15657234>

Williams M., Karamanis M., Luo Y., Seljak U., 2025b, Validating Se-
quential Monte Carlo for Gravitational-Wave Inference - Data Re-
lease, doi:10.5281/zenodo.15651282, <https://doi.org/10.5281/zenodo.15651282>

Table A1. Prior distributions used for inference in section 5.1. For definitions of each parameter, see Appendix E of Romero-Shaw et al. (2020). Table reproduced from Williams (2023).

Parameters	Prior	Bounds
\mathcal{M}	Uniform	[25, 35] M_{\odot}
q	Uniform	[0.125, 1.0]
d_L	Uniform in co-moving volume	[100, 2000] Mpc
α	Uniform	[0, 2π]
δ	Cosine	-
t_c	Uniform around trigger time	[-0.1, 0.1]
θ_{JN}	Sine	-
ψ	Uniform	[0, π]
ϕ_c	Uniform	[0, 2π]
a_i	Uniform	[0, 0.99]
θ_i	Sine	-
$\Delta\phi$	Uniform	[0, 2π]
ϕ_{JL}	Uniform	[0, 2π]

Wong K. W. k., Gabrié M., Foreman-Mackey D., 2023a, *J. Open Source
Softw.*, 8, 5021

Wong K. W. K., Isi M., Edwards T. D. P., 2023b, *Astrophys. J.*, 958, 129
pandas development team T., 2020, pandas-dev/pandas: Pandas,
doi:10.5281/zenodo.3509134, <https://doi.org/10.5281/zenodo.3509134>

APPENDIX A: SIMULATION DETAILS AND SAMPLER SETTINGS

In this section, we provide additional details about the simulated data and sampler settings used throughout this work. Any settings not specified here can be found in the accompanying data release ().

Table A1 details the priors used in section 5.1 when analysing the BBH signals in simulated data. The priors are based on those used in Williams et al. (2021) Williams et al. (2021). Injections were made using a custom script to ensure data consistency between the different analyses, the script is available in the data release. All signals simulated using IMRPhenomXPHM (Pratten et al. 2021) and injected into 512 seconds of Gaussian noise coloured according to the PSD of the desired detector. Analyses were performed using an 8-second window with two seconds on data after the trigger time.

Table A2 list the parameters used for simulating the BNS signal used in section 5.2. The signal was simulated using IMRPhenomPv2_NRTidalv2 (Hannam et al. 2014; Dietrich et al. 2019) and the functionality in bilby_pipe and injected into 128 seconds of coloured Gaussian noise. With these parameters and assuming O3 sensitivity, the matched filter SNR in each detector: 12.04 in H1, 14.14 in L1 and 8.56 in V1 and the overall network SNR is 20.45

The settings used for all analysis with dynesty are detailed in table A4, these settings have been used extensively in LVK analyses; see e.g. Abac et al. (2024). However, unlike the LVK analyses that use two or more sampling runs per analysis, we only use a single sampling run per injection. This reduces the computational cost but makes the results less robust to statistical variations from sampling.

Table A2. Parameters for BNS injection generated using IMRPhenomPv2_NRTidalv2. The chirp mass is defined in detector frame. For definitions of each parameter, see Appendix E of Romero-Shaw et al. (2020).

Parameters	Value
$\mathcal{M}[M_{\odot}]$	1.45
q	0.93
a_1	0.01
a_2	0.01
θ_1 [rad]	0.28
θ_2 [rad]	0.30
ϕ_{12} [rad]	0.48
ϕ_{JL} [rad]	0.33
d_L [Mpc]	45.00
δ [rad]	0.31
α [rad]	4.70
θ_{JN} [rad]	2.75
Ψ [rad]	0.03
ϕ [rad]	0.67
λ_1	149.35
λ_2	984.62
t_c [s]	0.06

Table A3. pocomc settings for various analyses described in section 5. For details about the different settings see the pocomc documentation.

Setting	BBH	BNS – fast	BNS – slow
n_effective	2000	1000	2000
n_active	1000	500	1000
n_steps	100	50	50
n_max_steps	1000	500	500
n_samples	10,000	5000	10,000

Table A4. dynesty settings for all analyses. For details about the different settings see dynesty and bilby documentation.

Setting	Value
nlive	1000
naccept	60
sample	acceptance-walk

APPENDIX B: ADDITIONAL RESULTS

In this section, we include additional results from the [probability-probability tests \(P-P tests\)](#) described in section 5.1. Figure B1 shows the results of three-detector P-P test with pocomc and figs. B2 and B3 show the results for the two- and three-detectors tests for dynesty. In all cases, the p -value is above 0.05, indicating the samplers pass the test.

This paper has been typeset from a $\text{\TeX}/\text{\LaTeX}$ file prepared by the author.

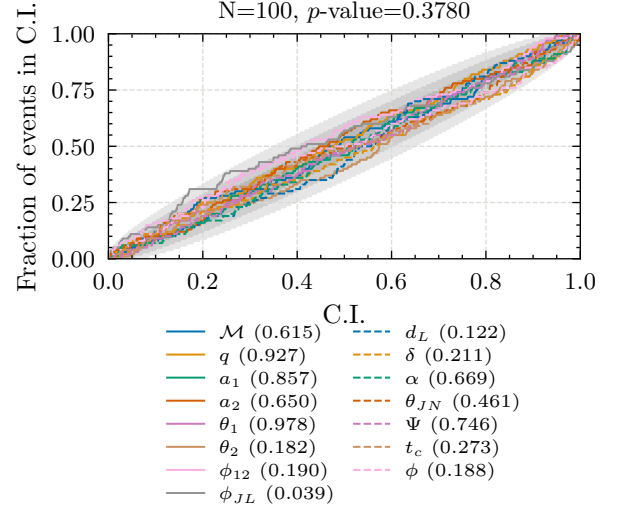


Figure B1. Probability-probability plot obtained using pocomc to analyse 100 simulated BBH signals in three-detector network consisting of LIGO Hanford, LIGO Livingston and Virgo. The shaded regions denote the 1-, 2- and 3- σ bounds respectively. Per-parameter p -values are quoted, as well as the combined p -value computed using Fisher's method (Fisher 1970).

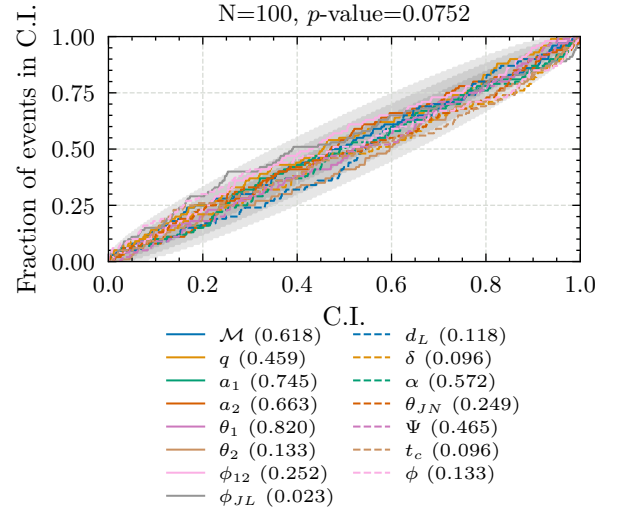


Figure B2. Probability-probability plot obtained using dynesty to analyse 100 simulated BBH signals in three-detector network consisting of LIGO Hanford, LIGO Livingston and Virgo. The shaded regions denote the 1-, 2- and 3- σ bounds respectively. Per-parameter p -values are quoted, as well as the combined p -value computed using Fisher's method (Fisher 1970).

Table B1. Comparison of the total number of likelihood evaluations, wall times and likelihood evaluation per sample when analysing a GW190425-like BNS using pocomc and dynesty with two-detector network. All analyses were run using 16 CPU cores and results are averaged over two runs. The equivalent results for a two-detector network are shown table 1.

Sampler	Precession	Tides	Likelihood evaluations	Wall time [min]	Likelihood evaluations per sample
dynesty	✗	✗	3.7×10^7	199.6	7530
pocomc	✗	✗	3.1×10^6	23.72	748.6
dynesty	✗	✓	3.0×10^7	181.4	5479
pocomc	✗	✓	4.2×10^6	35.78	1002
dynesty	✓	✗	2.9×10^7	129.7	5942
pocomc	✓	✗	6.3×10^6	43.75	1895
dynesty	✓	✓	2.5×10^7	169.9	4660
pocomc	✓	✓	1.8×10^7	143.6	2389

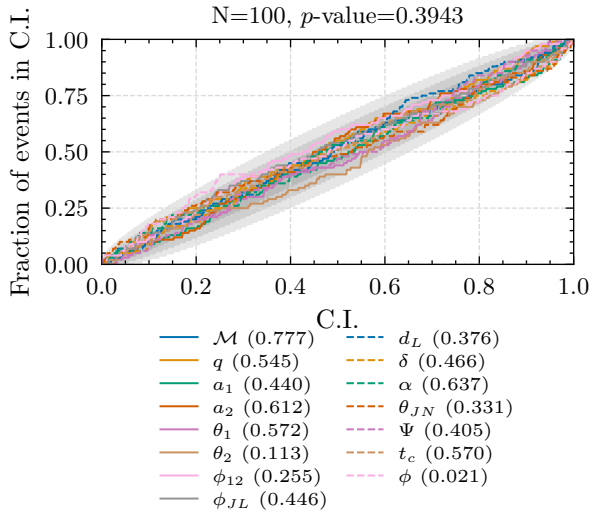


Figure B3. Probability-probability plot obtained using dynesty to analyse 100 simulated BBH signals in two-detector network consisting of LIGO Hanford and LIGO Livingston. The shaded regions denote the 1-, 2- and 3- σ bounds respectively. Per-parameter p -values are quoted as well as the combined p -value computed using Fisher's method (Fisher 1970).

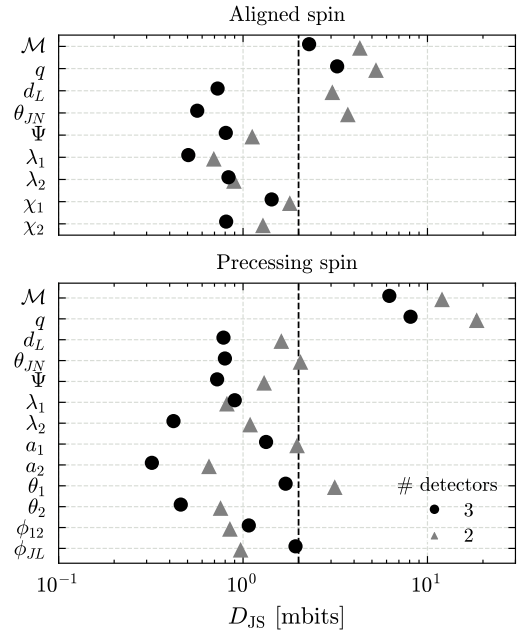


Figure B4. Mean JSD in millibits between posterior distributions obtained with dynesty and pocomc when analysing a simulated BNS signal as described in section 5.2. Results are shown for analyses with aligned and precessing spins, tidal effects, and for two- and three-detectors networks. The JSD is computed 10 times per analysis using 5000 samples and the error bars show the standard deviation. The parameters are defined in table A1. The vertical dashed line shows the threshold proposed in Ashton & Talbot (2021)